

Three Dimensional Cluster Analysis for Atom Probe Tomography Using Ripley's K-function and Machine Learning

Galen B. Vincent^{a, b}, Andrew P. Proudian^b, and Jeramy D. Zimmerman ^{*b}

^aDepartment of Applied Mathematics and Statistics, Colorado School of Mines, Golden, CO 80401, USA

^bDepartment of Physics, Colorado School of Mines, Golden, CO 80401, USA

January 1, 2022

Abstract

The size and structure of spatial molecular and atomic clustering can significantly impact material properties and is therefore important to accurately quantify. Ripley's K-function ($K(r)$), a measure of spatial correlation, can be used to perform such quantification when the material system of interest can be represented as a marked point pattern. This work demonstrates how machine learning models based on $K(r)$ -derived metrics can accurately estimate cluster size and intra-cluster density in simulated three dimensional (3D) point patterns containing spherical clusters of varying size; over 90% of model estimates for cluster size and intra-cluster density fall within 11% and 18% error of the true values, respectively. These $K(r)$ -based size and density estimates are then applied to an experimental APT reconstruction to characterize MgZn clusters in a 7000 series aluminum alloy. We find that the estimates are more accurate, consistent, and robust to user interaction than estimates from the popular maximum separation algorithm. Using $K(r)$ and machine learning to measure clustering is an accurate and repeatable way to quantify this important material attribute.

keywords: Ripley's K-function, spatial statistics, aggregation, cluster detection, atom probe tomography, machine learning

*Corresponding Author. Email: jdzimmer@mines.edu

1 Introduction

Understanding clustering (spatial aggregation) of certain species in materials is critical for studying structure-property relationships in materials science. Properties ranging from mechanical hardness to electronic transport can be impacted by molecular or atomic aggregation [1, 2, 3, 4]. The size, shape, spacing, and other defining characteristics of such aggregation play a crucial roll in determining its impact on material properties; for example, 7000 series aluminum alloys containing zinc and magnesium, which are commonly used in aerospace applications, are known to have higher strength when alloying elements aggregate into clusters of appropriate size [5]. Because of their impact on material properties, characterizing cluster properties such as size, intra-cluster atomic concentration, background atomic concentration, and cluster spacing is of great utility to the materials science community. Atom Probe Tomography (APT), which produces sub-nanometer resolution 3-dimensional (3D) tomograms consisting of the (x, y, z) positions and mass-to-charge-state ratios of each ion collected from a material sample, allows for detailed analysis of nanoscale morphology [6]. In this work, we develop a procedure for accurate quantification of clusters in APT data using tools from point pattern spatial statistics.

There are numerous existing cluster search algorithms designed to identify areas of aggregation in APT reconstructions [7, 8, 9, 10, 11]. These methods generally rely on one or more initialization parameters from the user. For example, the maximum separation algorithm (MSA), one of the most commonly used cluster detection algorithms in the APT community, requires the initialization of two crucial parameters: d_{\max} (the maximum distance between two points in a cluster) and N_{\min} (the minimum number of points in a cluster) [12]. This algorithm’s output is highly sensitive to the choice of these two parameters [13, 14], and while there are general guidelines for this parameter selection [10, 12], the procedures are still subjective. This user-guided parameter selection is typical of other cluster detection algorithms as well [7, 9]. The dependence of these algorithms on user judgment to select these critical parameters compromises the reproducibility of their results.

Other methods have been developed to analyze clustering in APT reconstructions based on spatial statistics, using tools like the nearest neighbor distance distribution or radial distribution function [15, 16, 17, 18, 19]. One of the most powerful spatial statistics tools for detection of clustering is Ripley’s K-Function ($K(r)$), which summarizes spatial correlation in point patterns at a variety of length scales [20, 21]. $K(r)$ has been used to estimate the size of circular point clusters in 2D point patterns [22, 23, 24], but there has been minimal work exploring how this extends to 3D (*e.g.* for APT data analysis applications). $K(r)$ -based cluster size estimates are independent of initialization parameters, and are thus largely independent of the user; this makes them attractive as a consistent tool for characterizing clusters.

In this work, we develop a general method using $K(r)$ to characterize clusters in 3D spatial point patterns, with a specific focus on application to APT data, where atoms or molecules can be represented by points in a pattern. We use summarizing metrics from $K(r)$ measured on simulated 3D point patterns with spherical clusters to train machine learning models to estimate cluster size, intra-cluster point concentration, and background point concentration; these models produce accurate estimates for point patterns with non-uniform cluster size,

sporadic cluster spacing, and significant background point concentration. Applying the method to an APT reconstruction of a 7000 series AlMgZn alloy, we compare the resultant size and concentration estimates to similar estimates obtained using the MSA and find that the $K(r)$ -based estimates offer a significant improvement over those from the MSA. This procedure is independent of user-defined initialization parameters, providing an accurate, reliable, and consistent method to characterize clustering in material systems.

2 Background and Methods

2.1 Ripley’s K-function

Ripley’s K-function measures correlations between point locations at different length scales in a point pattern. It is defined as the expected number of additional points that lie within a radius r of a typical point in the pattern, normalized by the global intensity (*i.e.* points per unit volume) of the pattern [20]. Given an observed point pattern, $K(r)$ is calculated as

$$K(r) = \frac{1}{\lambda m} \sum_{i=1}^m \sum_{\substack{j=1 \\ j \neq i}}^m I\{d_{ij} < r\} e_{ij}(r), \quad (1)$$

where m is the number of points in the pattern, λ is the intensity of the point pattern ($m/\text{volume of pattern}$), d_{ij} is the distance between points i and j , I is the indicator function (*i.e.* $I\{d_{ij} < r\}$ is equal to one for $d_{ij} < r$ and equal to zero otherwise), and $e_{ij}(r)$ is an edge correction weight that adjusts for bias introduced by points that lie within a distance r of the edge of the pattern [21]. $K(r)$ is typically estimated at a finely spaced series of r values over a length scale of interest.

In this study, we use $K(r)$ to analyze marked point patterns where each point is assigned a categorical label or “mark” from one of two categories: A or B . We denote the total number of points in a pattern as m , and the fraction of point marked type- A as η , $0 < \eta < 1$. The set of all point positions in a pattern, disregarding their marks, is called the underlying point pattern (UPP). For the remainder of this work, we measure $K(r)$ on only the subset of type- A points within the UPP; this allows us to study the spatial structure of type- A points within the UPP.

Random relabeling of the UPP allows for estimation of the expected $K(r)$ signal for randomly distributed marks within the pattern. Random relabeling is a process in which $K(r)$ is measured on a random subset of $m\eta$ points from the UPP. Repeating this process of subset selection and measurement many times creates an envelope showing where $K(r)$ measurements of randomly marked versions of the UPP are expected to fall; the median of this envelope is the expected $K(r)$ signal for a random distribution of type- A points within the UPP. If the $K(r)$ measurement from the originally observed point pattern ($K_{A\text{-obs}}(r)$) deviates significantly from this envelope, one may reasonably conclude that the distribution of type- A marks in the observed point pattern is not random [21]. The goal of this work is to make inferences about the structure of type- A marks within the UPP based on the behavior of this deviation from the random signal.

We use a transformed version of $K(r)$, which we call $T(r)$, to directly measure the deviation of the observed signal from the expected random signal:

$$T(r) = \sqrt{K_{\text{A-obs}}(r)} - \sqrt{K_{(N/2)}(r)}, \quad (2)$$

where $K_{(N/2)}(r)$ is the median of the $K(r)$ envelopes for N random relabelings of the UPP; this subtraction serves to center $T(r)$ around zero. The square roots in equation (2) serve to stabilize the variance of $T(r)$ across all r values [21]. A more detailed discussion of the procedure used to calculate $T(r)$ is provided in Section 1 of the SI.

2.2 K-Function-Derived Metrics

Single metrics from $K(r)$, such as the radius of maximal aggregation [23, 24] or functions of the derivatives of $K(r)$ [24], have been used to estimate cluster size in 2D point patterns. These single-metric-based estimators showed promising results for ideal clustered patterns (uniform cluster size, regular cluster spacing, low background point concentration), but began to fail as non-idealities were introduced. To build a more robust model for cluster size, intra-cluster point concentration, and background point concentration, we instead use five separate metrics based on $T(r)$. Each of the five metrics is a function of $T(r)$ or its derivatives. The derivatives are calculated using the central difference method, and maxima and minima are located using rolling local polynomial fit smoothing. Table 1 shows the name and description of each metric, and Figure 1 shows an example $T(r)$ result from a type-A clustered data set, its first three derivatives, and the location of each metric. R_{max} , Rd_{min} , and Rd_{max}^3 are correlated with cluster size [23, 24], while T_{max} and Td_{min} capture the strength of the $T(r)$ signal and how quickly it falls from its first peak - properties largely determined by intra-cluster and background point concentration.

Table 1: Name and Description of $T(r)$ Metrics

Name	Description
T_{max}	The value of $T(r)$ at its first maximum.
R_{max}	The r value where T_{max} occurs.
Td_{min}	The value of $T'(r)$ at its first minimum
Rd_{min}	The r value where Td_{min} occurs.
Rd_{max}^3	The r value at the first maximum of $T'''(r)$

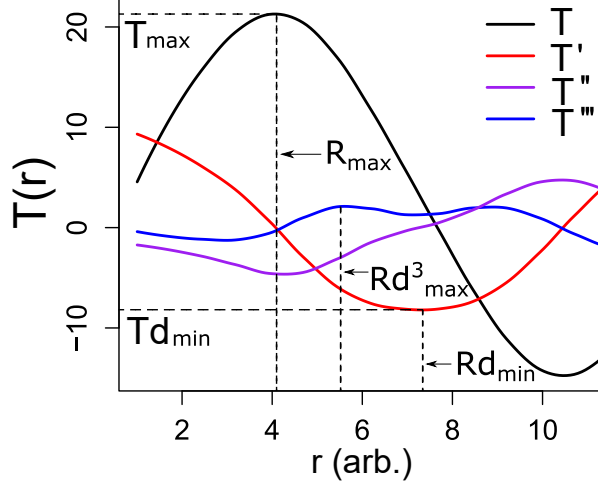


Figure 1: Example $T(r)$ measurement from a clustered point pattern (black line) along with its first three derivatives (colored lines). The metrics of interest are: T_{\max} , height of the first maxima of $T(r)$; R_{\max} , r value at the first maxima of $T(r)$; Td_{\min} , value of $T'(r)$ at its first minima; Rd_{\min} , r value at the first minima of $T'(r)$; Rd_{\max}^3 , r value at the first maxima of $T'''(r)$.

2.3 Simulation of Clustered Point Patterns

To develop our cluster characterization method, we use simulated 3D point patterns with spherically clustered type- A marks. The UPP in these simulations is taken to be the centers of 3D random close-packed (RCP) spheres; the diameter of these spheres defines the length unit for all simulated work in this study (denoted as “arb.”). This unit is scalable to any physical length, and is therefore somewhat arbitrary, but defined for consistency. The RCP structure emulates that of amorphous material systems; the points have a minimum nearest neighbor distance but do not follow any crystalline pattern at larger length scales. A previously developed algorithm [25] is used to generate realizations of RCP spheres within a $60 \times 60 \times 60$ arb. cubic volume. These UPPs have intensity of $\lambda_{\text{sim}} = 1.029$ points/arb.³.

Each point in the UPP is then marked as either type- A (cluster species) or type- B (host species). A type- A fraction of $\eta = 0.0511$ is used for all simulations in this study to match the measured η for the APT reconstruction analyzed in Section 4. Type- A points are assigned within the UPP to create spherical clusters in the following way: the radius R_c of each cluster within a pattern is a normally distributed random variable with mean μ_R and variance σ_R^2 (*i.e.* $R_c \sim N(\mu_R, \sigma_R^2)$); cluster centroids are defined by the centers of a scaled-up RCP sphere pattern and are then shifted in a uniformly random direction by random distance $d \sim |N(0, \sigma_C^2)|$; the intra-cluster concentration of type- A points (*i.e.* type- A points in a cluster/total points in the same cluster) is denoted ρ_1 ; the background concentration of type- A points (*i.e.* type- A points outside of clusters/total points outside of clusters) is denoted ρ_2 . The number of clusters within any simulated point pattern is determined by a combination of these five parameters.

Note that the σ_R and σ_C parameters are reported alternatively as radius blur ($\beta = \sigma_R/\mu_R$) and position blur ($\xi = \sigma_C/\mu_{\text{sep}}$, where μ_{sep} is the average separation distance between cluster

centers before they are shifted). For simulations in this study, we constrain $\beta < 0.5$ to avoid point patterns where many clusters are assigned a negative radius (when this occurs, the cluster is omitted completely from the simulation). Similarly, we constrain $\xi < 0.2$ to avoid having many clusters overlap after shifting their positions.

Simulations were performed in R mainly using the `spatstat` [21] and `rapt` [26] packages. Example simulation workflow scripts are available as Supplemental Information and on GitHub [27]. A more detailed discussion of the cluster simulation process can be found in Section 2 of the SI.

3 Simulation Results

3.1 Weighted Radius

The mean cluster radius μ_R is difficult to estimate using $T(r)$ metrics when the clusters within a single sample vary in size (*i.e.* $\beta \neq 0$) because larger clusters impact $K(r)$ (and therefore $T(r)$) disproportionately more than smaller clusters. Larger clusters (1) occupy a larger volume in the point pattern than the smaller clusters, and therefore contribute a “large cluster” signal to $K(r)$; (2) contain more points than the smaller clusters, meaning that the “large cluster” signals dominate $K(r)$, which is an average signal over every point in the pattern. The impact of this in point patterns with mean μ_R and non-uniform cluster sizes is that $K(r)$ will behave similarly to that from a point pattern with uniform cluster radii μ_R^* , where $\mu_R^* > \mu_R$. This becomes an issue when trying to estimate μ_R , as $T(r)$ metrics can not distinguish between these two situations.

Henceforth, we use the weighted radius (R_w), which is a function of the distribution of radii in a point pattern that gives each cluster the same weight that it receives in $K(r)$. This quantity can be generally written as

$$R_w = \frac{\mathbb{E} \left[r \times \frac{4}{3} \pi r^3 \right]}{\mathbb{E} \left[\frac{4}{3} \pi r^3 \right]}, \quad (3)$$

where $\mathbb{E}[X]$ is the expected value of a random variable X . R_w can be interpreted as the weighted average radius of clusters in the pattern, where the weight on each cluster’s radius r is its corresponding volume $\frac{4}{3} \pi r^3$. We use normally distributed radii ($R_c \sim N(\mu_R, \sigma_R^2)$), which simplifies equation (3) to the closed form expression

$$R_w = \frac{\mu_R^4 + 6\mu_R^2\sigma_R^2 + 3\sigma_R^4}{\mu_R^3 + 3\mu_R\sigma_R^2}. \quad (4)$$

Because $K(r)$ directly measures R_w , which is a function of both μ_R and σ_R , it is impossible to individually extract μ_R or σ_R given only output from $K(r)$. We therefore build models to estimate R_w and leave the decoupling of μ_R and σ_R for future work.

3.2 Estimating Cluster Properties

In this section, we develop a model that uses the five $T(r)$ metrics introduced in Section 2.2 as predictors to estimate weighted radius (R_w), intra-cluster type- A point concentration (ρ_1), and background type- A point concentration (ρ_2) for a simulated clustered point pattern of interest.

The $T(r)$ metrics were explored by sweeping through each simulation parameter (μ_R , ρ_1 , ρ_2 , β , and ξ) individually, which revealed that the five $T(r)$ metrics relate to the simulation parameters nonlinearly and are significantly correlated, meaning that multicollinearity of the predictors would likely be an issue for a standard linear regression model. The full results of this exploration are provided in Section 3 of the SI.

To eliminate issues with correlation, we use principal component analysis to transform the $T(r)$ metrics into their standardized principal components (PCs) [28], and use these PCs as predictors in machine learning models for estimating R_w , ρ_1 , and ρ_2 . Machine learning allows us to capture the complex relationships between the $T(r)$ -metrics and clustering parameters. To train these models, we generated 10,000 sets of random cluster parameters selected from uniform distributions over the ranges shown in Table 2. For each parameter combination, we simulated 10 clustered point patterns according to the procedure outlined in Section 2.3, resulting in a total of 100,000 simulated patterns. This method of repeating simulations at each parameter combination was designed to capture variation between simulations with the same input parameters. The expected random $K(r)$ signal was measured based on 50,000 random relabelings of the UPP, and was then used to calculate $T(r)$ and the five $T(r)$ metrics for each of the 100,000 simulated point patterns. We then calculated the five standardized PCs based on these metrics. A summary of the variance explained by these standardized PCs can be found in Section 4 of the SI. This set of 100,000 parameter-PC pairings were used to train the R_w , ρ_1 , and ρ_2 models.

Table 2: Cluster Parameter Ranges

Parameter	Range
Cluster Radius (μ_R)	[2, 6.5] arb.
Intra-cluster Concentration (ρ_1)	[0.2, 1]
Background Concentration (ρ_2)	[0, 0.03]
Radius Blur (β)	[0, 0.5]
Position Blur (ξ)	[0, 0.2]

The “no free lunch theorem” states that no single type of model will perform best for every data set [29]. Therefore, we tested three separate popular regression models appropriate for this type of analysis: a generalized linear model (GLM), a random forest model (RF), and a Bayesian regularized neural network (BRNN) model. To compare these options, we used a testing data set of 25,000 simulated clustered point patterns, each with a unique set of parameters selected from uniform distributions over the same ranges shown in Table 2.

We trained separate GLM, RF, and BRNN models for each parameter R_w , ρ_1 , and ρ_2 in R using the `caret` package [30] and 10-fold cross-validation. The best model for each parameter was selected as the one with the smallest root mean square error of prediction

(RMSEP) for the testing data set. These RMSEP values are shown in Table 3; the BRNN model performed best for all three parameters.

Table 3: RMSEP for Different Models and Parameters

		R_w	ρ_1	ρ_2
	GLM	0.4678	0.0875	0.00549
RMSEP	BRNN	0.4142	0.0559	0.00372
	RF	0.4272	0.0569	0.00381

Figure 2 summarizes the performance of these BRNN models on the testing data set of 25,000 simulations. Figure 2(a) shows the true simulated values of R_w versus the corresponding model estimates; the colors correspond to the percent error percentiles of these estimates (*e.g.* the 50% of estimates with lowest percent error are shown in red). Figure 2(b) shows the percent error of each estimate sorted in ascending order to easily determine what percent of model estimates fall below a certain percent error (*e.g.* 50% of estimates fall within 4% error). Figures 2(c,d) show similar plots for the ρ_1 testing data estimates from the BRNN model. Figures 2(e,f) show similar plots for the ρ_2 testing data estimates from the BRNN model, except that absolute error is used in place of percent error because $\rho_2 \approx 0$ in many of the simulated point pattern leads to very large percent errors.

In an auxiliary simulation study, we used the same process described above to train models for simulated point patterns with uniform cluster radii ($\beta = 0$). These models have much higher predictive ability than the models presented above for non-uniform cluster size and are detailed in Section 5 of the SI.

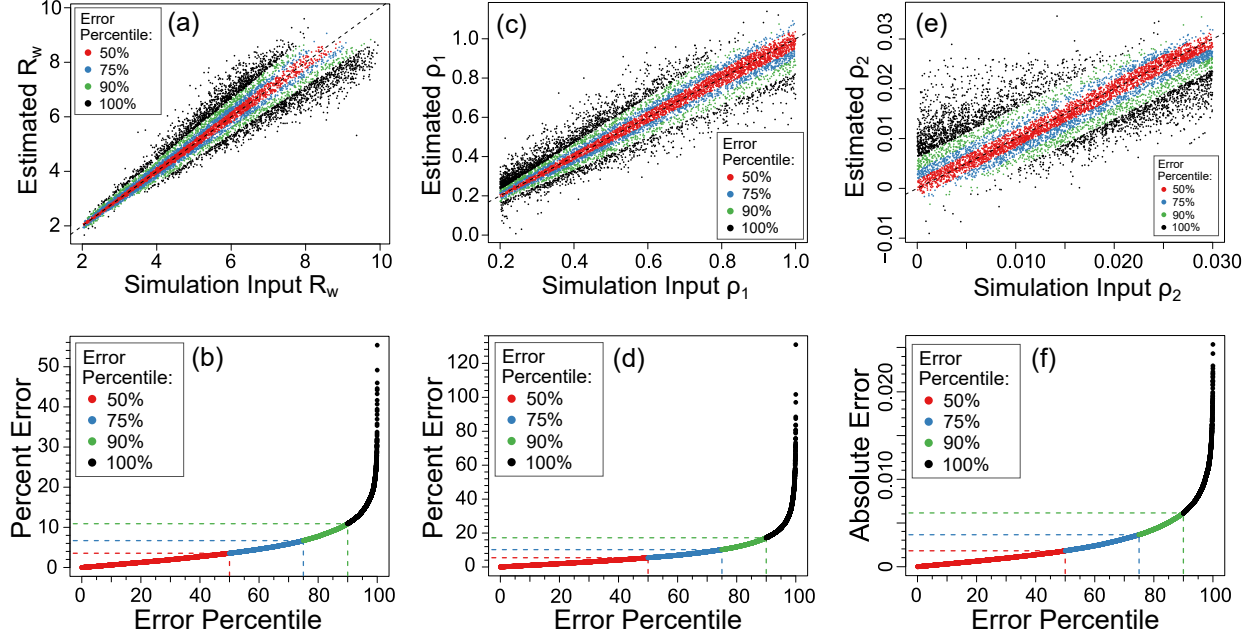


Figure 2: Results from the BRNN models of weighted radius (R_w), intra-cluster concentration (ρ_1), and background concentration (ρ_2); (a, c, e) Model estimates versus corresponding input simulated values for R_w , ρ_1 , and ρ_2 , respectively. Colors correspond to different error percentiles of the estimates (percent error for R_w and ρ_1 , absolute error for ρ_2); (b, d, f) Ordered error in testing data estimates for R_w , ρ_1 , and ρ_2 , respectively.

3.3 Discussion of Simulation Results

Table 3 shows that the BRNN model has the smallest RMSEP on the testing data set for R_w , ρ_1 , and ρ_2 estimates. Figure 2 shows that for the R_w model, 90% of estimates from this BRNN model fall below 11% error; for the ρ_1 model, 90% of estimates fall below 18% error; and for the ρ_2 model, 90% of estimates fall within 0.007 (absolute) of the true parameter value. These results are promising for the R_w and ρ_1 models, but less so for the ρ_2 model.

We have shown that precise and accurate characterization of cluster size and intra-cluster concentration using $K(r)$ is possible even in non-ideal cluster configurations (non-uniform cluster radii, irregular cluster spacing, and significant background point concentrations). It is noteworthy that the ρ_1 model was able to perform well even in these non-ideal situations, as $K(r)$ is not conventionally used as a measure of this quantity. The relatively poor performance of the ρ_2 model shows that the $T(r)$ metrics alone are weak predictors of the background point concentration of a clustered point pattern; this occurs because $K(r)$ contains more information about areas of high point concentration (*i.e.* clusters) and less information about areas of low point concentration (*i.e.* the space between clusters).

Cluster simulation studies are intrinsically limited by the parameters and simulation techniques, so we included a large range of clustering behaviors to cover many potential experimental outcomes; however, additional non-idealities could be explored, such as non-spherical clusters, non-uniform intra-cluster concentrations, or aberrations from the APT analysis and reconstruction processes. Furthermore, measures from other spatial statistics

functions would likely supplement the $T(r)$ -metrics to improve cluster parameter estimates. For example, the nearest-neighbor function $G(r)$ and empty-space function $F(r)$ measure small scale interactions in point patterns [21], which would be particularly useful for increasing the performance of the model for ρ_2 .

4 Application to Experimental Data

In this section, we analyze an APT reconstruction of a 7000 series aluminum alloy with primary alloying constituents of magnesium and zinc (AlMgZn), a material commonly used in aerospace applications. Mg and Zn clustering of appropriate size and density in these alloys has been shown to increase material strength [5]. The reconstruction we analyze is from an APT sample run at 30 K in ultraviolet laser pulsing mode at 250 kHz. We apply our cluster characterization method to estimate the size and density of MgZn clusters present in the sample and compare these estimates to similar estimates obtained from the MSA over a variety of input parameter combinations. The precise experimental details behind this APT reconstruction are important to experimental work, but are outside the scope of this paper because our main goal is to address the efficacy of cluster property estimation within a reconstruction.

4.1 MgZn Cluster Parameter Estimates

After identifying and selecting (*i.e.* ranging) only Al, Mg, and Zn atoms from the APT reconstruction, it contains 1,185,847 atoms in a $34.89 \text{ nm} \times 40.32 \text{ nm} \times 36.09 \text{ nm}$ cuboid with atomic percentages (at%) of 94.89% Al, 2.78% Zn, and 2.33% Mg. The global intensity of the point pattern is $\lambda_{\text{APT}} = 23.36 \text{ points/nm}^3$.

It is typical in this type of alloy for Mg and Zn to cluster together [31], so for this analysis we treat Zn and Mg as a single aggregating species that makes up 5.11 at% of the reconstruction. Our $K(r)$ -based method could make independent estimates for each clustering species by training models using simulations containing multiple species, but for simplicity, we have chosen to look at the species in combination for this initial demonstration.

We only estimate R_w and ρ_1 for this data set, as these models from Section 3.2 have the strongest performance. To apply these models to the AlMgZn alloy APT reconstruction, we assume that MgZn clusters in the sample are spherical, have normally distributed radii, and have uniform intra-cluster concentration. It is crucial that the spatial structure of the training data be consistent with that of the experimental data to apply these models accurately. The validity of these assumptions are addressed in Section 6 of the SI.

The experimental reconstruction and simulated training point patterns have significantly different global intensities ($\lambda_{\text{APT}} = 23.36 \text{ points/nm}^3$, $\lambda_{\text{sim}} = 1.029 \text{ points/arb.}^3$, respectively), which could lead to spurious estimates of R_w and ρ_1 , as the experimental estimates would be made in a parameter space that the model has not trained on. The experimental data was therefore scaled by a factor of $\alpha = \sqrt[3]{\lambda_{\text{APT}}/\lambda_{\text{sim}}} = 2.832$; this scaling preserves the features of the reconstruction but brings them into a length scale that our models have been trained on. The estimates of R_w from this scaled reconstruction will be in simulation units (arb.); to get back to units of nm, the scaled R_w estimate can be divided by α . Intra-cluster

concentration ρ_1 is independent of scaling, so the ρ_1 estimate for the scaled reconstruction is a valid ρ_1 estimate for the original reconstruction.

We used the models trained in Section 3.2 to estimate R_w and ρ_1 by measuring $T(r)$ on Mg and Zn atoms using 50,000 random relabelings of the measured UPP, extracting the five $T(r)$ metrics, and calculating the standardized metric PCs. These PCs were then used to obtain estimates of R_w and ρ_1 for the scaled reconstruction. We used the training set to estimate uncertainty in these estimates by collecting the subsets of training data simulations that resulted in R_w and ρ_1 estimates close to the estimates from the scaled reconstruction (within 0.2 arb. R_w and 0.02 ρ_1), collecting the true R_w and ρ_1 parameters from this subset of simulations, then using these true values to construct 90% confidence intervals (CIs) for the true values of R_w and ρ_1 . The parameter estimates, along with the corresponding 90% CIs are provided in Table 4.

Table 4: MgZn Cluster Parameter Estimates

Parameter	R_w (arb.)	R_w (nm)	ρ_1
Estimate	5.192	1.834	0.212
90% CI	[4.915, 5.700]	[1.736, 2.013]	[0.171, 0.255]

4.2 Comparison to Maximum Separation Algorithm

It is informative to compare the estimates in Table 4 to estimates of the same parameters using the MSA, which is one of the most commonly used cluster identification tools in the APT community [12, 13, 14]. The MSA requires two user-defined input parameters: d_{\max} , the maximum distance between two points in a cluster, and N_{\min} , the minimum number of points in a cluster [13]. There are two other parameters used for enveloping background points into clusters: L and E ; but these parameters do not impact algorithm output significantly and are usually both set equal to d_{\max} , which is what we do here [13]. To perform the MSA in this study, we used the `msa()` function within the `rapt` package [26].

The MSA only identifies which points reside in which clusters; to estimate ρ_1 and cluster size, further analysis is required. To estimate ρ_1 for each cluster identified by the MSA, we use the estimator:

$$\hat{\rho}_1 = \frac{\text{number of type-A points in cluster}}{\text{total number of points in cluster}}. \quad (5)$$

To estimate cluster radius for each cluster identified by the MSA, we use the estimator detailed in [32]:

$$\hat{R}_c = \sqrt{\frac{5}{3} \sum_{i=1}^n r_i^2}, \quad (6)$$

where n is the number of type-A points in the cluster and r_i is the distance between point i and the cluster center of mass.

We ran the MSA on the scaled version of the AlMgZn reconstruction using a range of d_{\max}

and N_{\min} parameters, as recommended by the analysis of Vaumousse, et al. [12]. For each version of the MSA, the intra-cluster concentration ρ_1 and mean cluster radius R_c and of all identified clusters in the sample were estimated using equations (5) and (6), respectively. A figure showing the mean R_c estimate as a function of d_{\max} and N_{\min} is provided in Section 7 of the SI. Using the estimated R_c for each MSA parameter combination, the weighted radius of the reconstruction R_w was then calculated using equation (3). Figure 3 shows these MSA estimates for R_w and mean ρ_1 of the reconstruction as a function of d_{\max} and N_{\min} along with the $K(r)$ -based estimates and 90% CIs from Table 4.

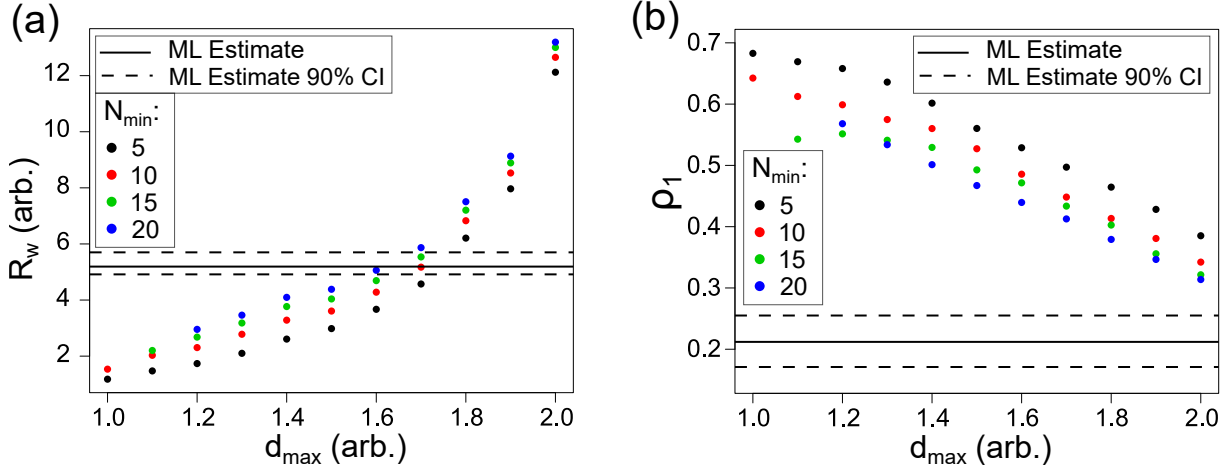


Figure 3: Maximum separation algorithm estimates for (a) weighted radius R_w and (b) mean intra-cluster concentration ρ_1 for clusters in the scaled AlMgZn alloy APT reconstruction, shown as a function of d_{\max} and N_{\min} . Solid black lines are estimates from $K(r)$ -based machine learning (ML) model. Dashed black lines are the 90% CI for the ML model estimates.

To compare the behavior of these $K(r)$ -based estimates with those from the MSA, we use results from simulated clustered data where the true values of R_w and ρ_1 are known. We simulated 500 clustered point patterns with cluster species fraction $\eta = 0.0511$ and parameters $\mu_R = 4.5$, $\beta = 0.238$ ($R_w = 5.192$), $\rho_1 = 0.212$, $\rho_2 = 0.03$, and $\xi = 0$, and estimated R_w and ρ_1 for each of these simulations using both our $K(r)$ -based machine learning estimates and estimates from the MSA over the same range of d_{\max} and N_{\min} parameters used in Figure 3. Note that the simulated cluster parameters match those measured from the reconstruction (Table 4). Figure 4 shows the results from this comparison; the true values for R_w and ρ_1 are shown as red dashed lines, the machine learning (ML) estimates of mean and 90% CIs are shown as black lines, and the MSA estimates are shown as colored dots.

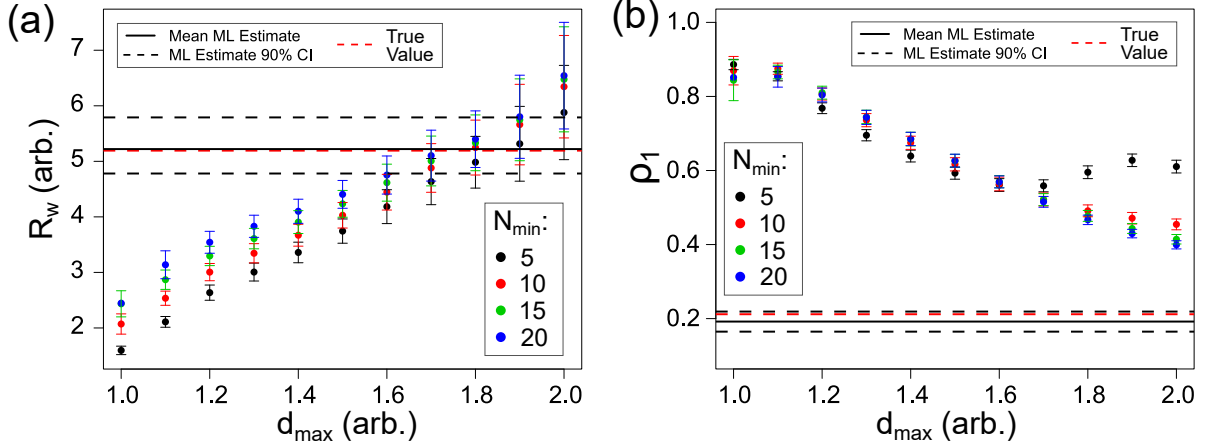


Figure 4: Maximum separation algorithm estimates for (a) weighted radius R_w and (b) mean intra-cluster concentration ρ_1 for clusters in simulated point patterns with known $R_w = 5.192$, $\rho_1 = 0.212$, $\rho_2 = 0.03$, $\xi = 0$. True values are shown as red dashed lines. $K(r)$ -based machine learning model estimates are shown as black lines with corresponding 90% CIs shown as black dashed lines.

4.3 Discussion of Experimental Results

Figure 3 shows that cluster property estimates of MgZn clustering in the reconstruction based on the MSA are highly dependent on d_{\max} and N_{\min} , and are especially sensitive to d_{\max} . Over the input parameter ranges swept, R_w estimates ranged between 1 and 13 arb., while ρ_1 estimates ranged between 0.7 and 0.3. The $K(r)$ -based R_w estimate shown in Table 4 falls in line with the MSA R_w estimates for certain parameter combinations ($d_{\max} \approx 1.7$, $N_{\min} \approx 10$), but the $K(r)$ -based ρ_1 estimate shown in Table 4 does not match the MSA estimates for any d_{\max} and N_{\min} combination tried.

When tested on simulated data with similar morphology to the reconstruction, the $K(r)$ -based machine learning estimates match the true values of R_w and ρ_1 closely with small variance. Similar to the experimental data, the MSA estimates for the simulated data vary significantly based on input parameter selection, only agree with the true value of R_w for a select few parameter combinations, and fail to agree with the true value of ρ_1 for any input parameter combination tried. It is important to note that there was no d_{\max}/N_{\min} combination that provided simultaneously accurate estimation of both R_w and ρ_1 , meaning that there is a fundamental disconnect between the clustering morphology identified by the MSA and the true clustering morphology of the system. Figures 3 and 4 show the similarities in behavior between the $K(r)$ -based and MSA estimation methods performed on the experimental and simulated data. The accuracy and precision of the $K(r)$ -based estimates for R_w and ρ_1 for the simulated data paired with the agreement in estimate behavior between simulation and experimental data leads to the conclusion that the $K(r)$ -based estimates agree closely with the true values of R_w and ρ_1 in the reconstruction and should be trusted above the estimates calculated from the MSA.

The consistent underestimation of the true value of ρ_1 in the simulated data (and likely

the experimental data) by the MSA estimator is due to a high concentration of background cluster type points (*i.e.* a large ρ_2 value). These background type-*A* points are randomly distributed through the point pattern, so if their concentration is high, some are bound to fall within d_{\max} of the edge of a cluster. The MSA then includes these points as part of the identified cluster, resulting in small “arms” of background type-*A* points extruding from the true cluster spheres. These arms contain few type-*B* points, so the clusters have a higher proportion of type-*A* points, resulting in an upward bias of the ρ_1 estimate. If d_{\max} is increased, these arms smooth out and more type-*B* points are enveloped into the cluster, resulting in lower estimates of ρ_1 . This explanation is consistent with Figure 4(b), which shows the MSA ρ_1 estimates consistently overestimate the true value of ρ_1 , but decrease towards the true value as d_{\max} is increased. Users of the MSA should be especially careful in point patterns with high background concentration, which are common in APT data.

A drawback to simulation-trained machine learning parameter estimation methods is that they only work well when the training data is consistent with the experimental data being analyzed. In this specific case, this idea corresponds to the cluster simulations agreeing with the morphology of a material. In contrast, the MSA can return clustering information for any morphology, which can sometimes be useful. However, Figures 3 and 4 clearly show that the estimates derived from the MSA are highly variable based on user-input parameters, while $K(r)$ -based estimates provide significantly greater accuracy and confidence. By expanding simulations to include a more diverse range of clustering behaviors, it should be possible to obtain machine learning models that outperform the MSA on most types of morphologies. The use of point pattern measurement tools other than $K(r)$ should further increase the accuracy and reliability of these models.

5 Conclusion

Machine learning models based on metrics derived from Ripley’s K -function can estimate cluster properties including size and intra-cluster concentration with high accuracy in simulated 3D data sets with non-ideal conditions. Over 90% of $K(r)$ -based estimates for R_w and ρ_1 fell within 11% and 18% error of the true values, respectively. We applied this estimation method to an APT reconstruction of a 7000 series Al alloy to estimate R_w and ρ_1 for MgZn clusters and compared these estimates to those from the popular MSA method, showing that estimates from the MSA strongly depend on user input parameters, while the $K(r)$ -based estimates are more consistent. Using simulated data similar in morphology to the reconstruction, we then showed that the $K(r)$ -based estimates are likely more accurate and consistent with the true values of R_w and ρ_1 than those from the MSA method. These demonstrations show how this procedure for quantifying clustering in 3D point patterns can measure material morphologies more consistently and accurately than existing methods. Understanding the connection between a material’s morphology and its properties is crucial for optimizing current materials and developing new ones; the procedures developed in this work can be used to further develop accurate structure-property relationships. The results here justify further investigation into the use of machine learning and spatial statistics to characterize tomographic data.

6 Acknowledgements

The authors would like to thank Stephan Gerstl and the Scientific Center for Optical and Electron Microscopy at ETH Zürich for supplying the AlMgZn APT reconstruction analyzed in this work. The authors would additionally like to thank Matthew B. Jaskot and Paul Niyonkuru for their manuscript feedback and suggestions.

7 Author Contributions

GBV - Method development, simulation development and execution, analysis of experimental data, interpretation of results, primary manuscript writing and editing.

APP - Method development, manuscript editing.

JDZ - Method development, interpretation of results, manuscript editing.

8 Funding Sources

Work by GBV, APP, and JDZ was supported by the U.S. Department of Energy, Office of Science, Basic Energy Sciences under Award DE-SC0018021 and by funding from Universal Display Corporation. Funding sources had no involvement in this work.

9 Competing Interests

The authors have no competing interests to declare.

References

- [1] Kwan H Lee, Paul E Schwenn, Arthur RG Smith, Hamish Cavaye, Paul E Shaw, Michael James, Karsten B Krueger, Ian R Gentle, Paul Meredith, and Paul L Burn. Morphology of all-solution-processed bilayer organic solar cells. *Advanced Materials*, 23(6):766–770, 2011.
- [2] Yang Yang, Yijian Shi, Jie Liu, and Tzung-Fang Guo. The control of morphology and the morphological dependence of device electrical and optical properties in polymer electronics. *Research Signpost*, 2003.
- [3] Chifei Wu, Kazue Mori, Yoshio Otani, Norikazu Namiki, and Hitoshi Emi. Effects of molecule aggregation state on dynamic mechanical properties of chlorinated polyethylene/hindered phenol blends. *Polymer*, 42(19):8289–8295, 2001.
- [4] Yu Hang Chui, Gregory Grochola, Ian K Snook, and Salvy P Russo. Molecular dynamics investigation of the structural and thermodynamic properties of gold nanoclusters of different morphologies. *Physical Review B*, 75(3):033404, 2007.
- [5] A Deschamps, F Livet, and Y Brechet. Influence of predeformation on ageing in an al–zn–mg alloy. microstructure evolution and mechanical properties. *Acta materialia*, 47(1):281–292, 1998.
- [6] David N Seidman and Krystyna Stiller. An atom-probe tomography primer. *Mrs Bulletin*, 34(10):717–724, 2009.
- [7] Emmanuelle A Marquis and Jonathan M Hyde. Applications of atom-probe tomography to the characterisation of solute behaviours. *Materials Science and Engineering: R: Reports*, 69(4-5):37–62, 2010.
- [8] P Felfer, AV Ceguerra, SP Ringer, and JM Cairney. Detecting and extracting clusters in atom probe data: A simple, automated method using voronoi cells. *Ultramicroscopy*, 150:30–36, 2015.
- [9] W Lefebvre, T Philippe, and F Vurpillot. Application of delaunay tessellation for the characterization of solute-rich clusters in atom probe tomography. *Ultramicroscopy*, 111(3):200–206, 2011.
- [10] Leigh T Stephenson, Michael P Moody, Peter V Liddicoat, and Simon P Ringer. New techniques for the analysis of fine-scaled clustering phenomena within atom probe tomography (apt) data. *Microscopy and Microanalysis*, 13(6):448–463, 2007.
- [11] Jennifer Zelenty, Andrew Dahl, Jonathan Hyde, George DW Smith, and Michael P Moody. Detecting clusters in atom probe data with gaussian mixture models. *Microscopy and Microanalysis*, 23(2):269–278, 2017.
- [12] D Vaumousse, A Cerezo, and PJ Warren. A procedure for quantification of precipitate microstructures from three-dimensional atom probe data. *Ultramicroscopy*, 95:215–221, 2003.

- [13] JM Hyde, EA Marquis, KB Wilford, and TJ Williams. A sensitivity analysis of the maximum separation method for the characterisation of solute clusters. *Ultramicroscopy*, 111(6):440–447, 2011.
- [14] Yan Dong, Auriane Etienne, Alex Frolov, Svetlana Fedotova, Katsuhiko Fujii, Koji Fukuya, Constantinos Hatzoglou, Evgenia Kuleshova, Kristina Lindgren, Andrew London, et al. Atom probe tomography interlaboratory study on clustering analysis in experimental data using the maximum separation distance approach. *Microscopy and Microanalysis*, pages 1–11, 2018.
- [15] T Philippe, S Duguay, G Grancher, and D Blavette. Point process statistics in atom probe tomography. *Ultramicroscopy*, 132:114–120, 2013.
- [16] Michael P Moody, Leigh T Stephenson, Anna V Ceguerra, and Simon P Ringer. Quantitative binomial distribution analyses of nanoscale like-solute atom clustering and segregation in atom probe tomography data. *Microscopy research and technique*, 71(7):542–550, 2008.
- [17] T Philippe, S Duguay, and D Blavette. Clustering and pair correlation function in atom probe tomography. *Ultramicroscopy*, 110(7):862–865, 2010.
- [18] T Philippe, F De Geuser, S Duguay, W Lefebvre, O Cojocar-Mirédin, Grégory Da Costa, and D Blavette. Clustering and nearest neighbour distances in atom-probe tomography. *Ultramicroscopy*, 109(10):1304–1309, 2009.
- [19] RKW Marceau, LT Stephenson, CR Hutchinson, and SP Ringer. Quantitative atom probe analysis of nanostructure containing clusters and precipitates with multiple length scales. *Ultramicroscopy*, 111(6):738–742, 2011.
- [20] Philip M Dixon. Ripley’s k function. *Wiley StatsRef: Statistics Reference Online*, 2014.
- [21] Adrian Baddeley, Ege Rubak, and Rolf Turner. *Spatial point patterns: methodology and applications with R*. Chapman and Hall/CRC, 2015.
- [22] Thibault Lagache, Gabriel Lang, Nathalie Sauvonnet, and Jean-Christophe Olivo-Marin. Analysis of the spatial organization of molecules with robust statistics. *PLoS One*, 8(12):e80914, 2013.
- [23] Arun Shivanandan, Jayakrishnan Unnikrishnan, and Aleksandra Radenovic. On characterizing protein spatial clusters with correlation approaches. *Scientific reports*, 6:31164, 2016.
- [24] Maria A Kiskowski, John F Hancock, and Anne K Kenworthy. On the use of ripley’s k-function and its derivatives to analyze domain size. *Biophysical journal*, 97(4):1095–1103, 2009.
- [25] Kenneth W Desmond and Eric R Weeks. Random close packing of disks and spheres in confined geometries. *Physical Review E*, 80(5):051305, 2009.

- [26] A.P. Proudian. Rapt: R for atom probe tomography. <https://github.com/aproudian2/rapt>, 2020.
- [27] G.B. Vincent. 3d cluster analysis vignette. <https://github.com/galenvincent/3D-Cluster-Analysis-Vignette>, 2020.
- [28] Ian Jolliffe. *Principal component analysis*. Springer, 2011.
- [29] Kevin P Murphy. *Machine learning: a probabilistic perspective*. MIT press, 2012.
- [30] Max Kuhn et al. Building predictive models in r using the caret package. *Journal of statistical software*, 28(5):1–26, 2008.
- [31] Gang Sha and Alfred Cerezo. Early-stage precipitation in al–zn–mg–cu alloy (7050). *Acta Materialia*, 52(15):4503–4516, 2004.
- [32] R Prakash Kolli and David N Seidman. Comparison of compositional and morphological atom-probe tomography analyses for a multicomponent fe-cu steel. *Microscopy and Microanalysis*, 13(4):272–284, 2007.